Age-Independent Oceanic Plate Thickness and Asthenosphere Melting from SS Precursor Imaging

Shuyang Sun[1]and Ying Zhou[1]

[1]Department of Geosciences, Virginia Tech, Blacksburg, VA 24061, USA

Key Points:

- SS precursors reveal depths of the lithosphere-asthenosphere boundary independent of seafloor age
- The oceanic lithosphere-asthenosphere boundary is a strong reflector and can be explained by 1.5%-2% of partial melt
- Large depth variations of the top and the bottom boundaries of the asthenosphere suggest a heterogeneous melting process

Corresponding author: Shuyang Sun, `sysun@vt.edu`

Abstract

The Earth's asthenosphere is a mechanically weak layer characterized by low seismic velocity and high attenuation. The nature of this layer has been strongly debated. In this study, we process twelve years of seismic data recorded at the global seismological network (GSN) stations to investigate SS waves reflected at the upper and lower boundaries of this layer in global oceanic regions. We observe strong reflections from both the top and the bottom of the asthenosphere, dispersive across all major oceans. The average depths of the two discontinuities are 120 km and 255 km, respectively. The SS waves reflected at the lithosphere and asthenosphere boundary are characterized by anomalously large amplitudes, which require ~12.5% reduction in seismic velocity across the interface. This large velocity drop can not be explained by a thermal cooling model but indicates 1.5%-2% localized melt in the oceanic asthenosphere. The depths of the two discontinuities show large variations, indicating that the asthenosphere is far from a homogeneous layer but likely associated with strong and heterogeneous small-scale convections in the oceanic mantle. The average depths of the two boundaries are largely constant across different age bands. In contrast to the half space cooling model, this observation supports the existence of a constant-thickness plate in oceanic regions with a complex and heterogeneous origin.

Plain Language Summary

In the plate tectonic theory, the outermost shell of the Earth consists of a small number of rigid plates (lithosphere) moving horizontally on the mechanically weak asthenosphere In oceanic regions, the lithosphere is thought to be formed by gradual cooling of the hot mantle. Therefore, the thickness of the plate depends on the age of the seafloor. The problem with the classic half space cooling model is that bathymetry and heat flow measurements at old seafloors do not follow its predicted age dependence. A modified theory, called the plate model, can better explain those geophysical observations by assuming additional heat at the base of an oceanic plate with a constant thickness of about 125 km. However, such a constant-thickness plate has not been observed in seismology. In this study, we image the asthenosphere boundaries using a global dataset of seismic waves reflected off the Earth's internal boundaries. We observe strong reflections from both the top and the bottom of the asthenosphere, across all major oceans. The amplitudes of these waves can be explained by 1.5%-2% of partial melt and the average boundary depths are independent of seafloor age. This observation supports the existence of a constant-thickness plate in the global oceans with a complex origin.

1 Introduction

In the plate tectonic theory, the outermost shell of the Earth consists of a small number of rigid plates (lithosphere) moving horizontally on the mechanically weak asthenosphere. The origin of the asthenosphere as well as the defining mechanism of its top and bottom rheological interfaces have been highly controversial (Fischer et al., 2010; Rychert et al., 2012; Kawakatsu & Utada, 2017; Fischer et al., 2020; Rychert et al., 2020; Karato, 1992; Gaherty & Jordan, 1995). The oceanic plates make up ∼70% of the Earth's surface and they have a relatively simple geological and tectonic history and therefore they are ideal for resolving these fundamental questions. The classic half-space cooling model predicts that the thickness of the thermal boundary layer as well as the depth of the ocean increase proportionally with the square root of the sea-floor age. While this simple conductive cooling model successfully explains the first-order observations in the oceans, bathymetry and heat flow measurements at seafloor older than ∼70 million years do not follow the age dependence predicted by the half space cooling model. The plate model, which assumes additional heat at the base of an oceanic plate with a constant thickness, successfully explains the flattening of sea floor depth and heat flow observations (Parsons & Sclater, 1977). However, such a constant-thickness plate has not been observed in seismology, and the exact source of the additional heat remains unclear, probably associated with small-scale convections (Richter, 1973; Richter & Parsons, 1975; Parsons & Sclater, 1977; Richards et al., 2020) or oceanic hotspots (Korenaga & Korenaga, 2008).

It is a general feature in global seismic surface wave studies that the high-velocity lid in oceanic regions becomes thicker with sea-floor age (French et al., 2013; James et al., 2014; Godfrey et al., 2017; Ma & Dalton, 2019). It has also been suggested that a plate model with additional heat at a constant depth of about 125 km fits surface wave observations (Maggi et al., 2006). Recent surface-wave studies suggest a small amount of melt is trapped within the entire low-velocity oceanic asthenosphere (Debayle et al., 2020), which might provide the additional heat required by the plate model. The depths of the lithosphere-asthenosphere boundary (LAB hereinafter) have also been studied using secondary seismic phases reflected or converted at the interface, including SS precursors (Rychert & Shearer, 2011; Schmerr, 2012; Tharimena et al., 2017), receiver functions (Li et al., 2000, 2004; Kawakatsu et al., 2009; Rychert & Shearer, 2009) and active source studies (Stern et al., 2015; Mehouachi & Singh, 2018). Those studies suggest large variations as well as an origin of the astheno-

sphere much more complex than gradual thermal variations with depth as predicted in the half space cooling model (D. Turcotte & Oxburgh, 1967). A variety of rheological mechanisms have been proposed, including a change in grain size (Faul & Jackson, 2005), seismic anisotropy (Karato & Wu, 1993; Beghein et al., 2014; Auer et al., 2015), elastically accommodated grain boundary sliding (Karato, 2012) and near melting (Yamauchi & Takei, 2016). The large velocity drop and high attenuation also make partial melt a dominant mechanism in many studies (Fischer et al., 2020; Rychert et al., 2020; Debayle et al., 2020; Stern et al., 2015; Mehouachi & Singh, 2018; Schmerr, 2012; Tharimena et al., 2017; Li et al., 2000, 2004; Kawakatsu et al., 2009). For example, a thin sublithosphere melt channel beneath the normal oceanic seafloor has been proposed for the equatorial Atlantic Ocean (Mehouachi & Singh, 2018).

The velocity increase at the base of the asthenosphere has been incorporated in the widely used 1-D global reference earth model, PREM, with about $\sim$7% of velocity increase across the 220-km discontinuity (Dziewonski & Anderson, 1981). A discontinuity at about this depth was first observed in Europe and North America (Lehmann, 1959, 1961; Hales et al., 1980) and later confirmed by studies using surface-wave dispersion measurements, underside seismic reflections, ScS reverberations and receiver functions (Goncz & Cleary, 1976; Vidale & Benz, 1992; Revenaugh & Jordan, 1991; Sacks et al., 1979). This discontinuity has been reported in continental regions and is also called the Lehmann discontinuity. However, many studies have concluded that the 220-km discontinuity is not global in nature and a reflection from this depth is missing in the global long-period stacks (Shearer, 1991; Gu et al., 2001; Deuss & Woodhouse, 2002, 2004; Schmerr & Garnero, 2006), which indicates that the existence of the discontinuity is either absent in oceanic regions, or there are large variations in the depth of this discontinuity.

In this paper, we analyze twelve years of long-period transverse component seismograms recorded at 151 GSN stations (Fig. S1) to investigate SS waves reflected at the top and the bottom of the asthenosphere in oceanic regions, namely, the $S_{\mathrm{LAB}}S$ wave reflected at the LAB and the $S_{220}S$ reflected at the bottom of the asthenosphere. We will interpret the low velocity zone (LVZ) between the two discontinuities observed in oceanic regions as the asthenosphere ("weak layer") as it roughly corresponds to the depth range of the global

LVZ in model PREM. This is the depth range where geotherm may exceed mantle solidus and partial melt occurs (D. L. Turcotte & Schubert, 2002).

2 Data & Methods

SS precursors are underside reflections from internal discontinuities and they arrive before the main SS waves which are reflected at the surface of the Earth. SS precursors are very sensitive to the structures of the interfaces at the reflection midpoints, about halfway between the earthquake and the station. They provide good data coverage in the global oceanic areas where seismic stations are sparse. In this study, we examine 32,369 broadband seismograms at 151 GSN station from 543 earthquakes occurred between January 2009 and December 2020 with SS-wave reflection points in oceanic regions (Figs 1 & 2). The moment magnitude of the earthquakes ranges from 6.0 to 8.0 such that SS precursors are excited by potentially sufficient seismic energy (Schmerr, 2012). We download seismograms from the Data Management Center at the Incorporated Research Institutions for Seismology (IRIS). The instrument responses are removed and the East-West and North-South component displacement seismograms are rotated to obtain the radial and transverse component seismograms.

The seismograms are band-pass filtered between 10 and 80 mHz and decimated to 0.1 second sampling interval. Seismograms with weak or complex SS waves due to source processes are discarded (Figs S2 & S3). Seismograms with noisy SS waves and precursors are also discarded (Fig. S3). This leaves 6,143 sets of transverse component seismograms with epicentral distances greater than 80°. We visually inspect seismograms for SS precursors, including $S_{\mathrm{LAB}}S$, $S_{220}S$, $S_{410}S$ and $S_{660}S$. Clear $S_{\mathrm{LAB}}S$ arrivals are identified on 1,380 seismograms (about 22.5% of the entire dataset) from 144 stations and 395 earthquakes (Figs 1 & 2). The majority of the data with strong $S_{\mathrm{LAB}}S$ waves (981 out of 1380) have focal depths shallower than 45 km, and the epicentral distance varies between 80.1° and 176.3° with the majority larger than 100° (Fig. S1).

SS precursors from the 220-km discontinuity ($S_{220}S$) are observed on 2,756 seismograms. We are able to pick more $S_{220}S$ phases than $S_{\mathrm{LAB}}S$ phases from seismograms partly because many $S_{\mathrm{LAB}}S$ arrivals are too close to the main SS wave arrivals and they are not

used in this study to avoid strong phase interferences. The $S_{\mathrm{LAB}}S$ and $S_{220}S$ signals can be both clearly observed on 1,021 of seismograms. There is no apparent geographic pattern associated with the presence (or absence) of the SS precursors (Fig. 2). The amplitudes of the secondary reflected waves are expected to be small, and the SS precursors are often below the noise level due to weak source radiation, small reflection coefficient and/or defocusing caused by mantle heterogeneities. For example, only about 30% of the recorded SS waves have clear SS precursors from the 410-km and the 660-km discontinuities in recent global studies (Guo & Zhou, 2020, 2021).

The observed SS precursors from the LAB ($S_{\mathrm{LAB}}S$) are characterized by large amplitudes that are comparable to the amplitudes of the mantle transition zone SS precursors $S_{410}S$ and $S_{660}S$ (Fig. 1). To investigate the velocity reduction across the LAB discontinuity, we construct 1-D reference models modified from PREM to include a large velocity drop in the asthenosphere (Fig. 3 & Fig. S4). We calculate synthetic seismograms based on traveling-wave mode summation (Liu & Zhou, 2016). The global centroid-moment-tensor (CMT) solutions and the USGS Preliminary Determination of Epicenters (PDE) source locations and origin times are used in the calculations of the 1-D synthetic seismograms. The synthetic seismograms are complete, including all seismic phases with exact amplitudes for earthquakes in 1-D earth models. The effects of incident angles on seismic amplitudes have been automatically accounted for. The synthetic seismograms are then processed using the same bandpass filter as applied to the observed seismograms. The differences in SS precursors between different models facilitate the identification of the $S_{\mathrm{LAB}}S$ and $S_{220}S$ waves on the observed seismograms (Fig. 3).

We measure the amplitudes of the SS precursors $S_{\mathrm{LAB}}S$, $S_{410}S$ and $S_{660}S$ at a period of 25 seconds. The measurements are made in the frequency domain using a 40-second window centered at the arrival time of the SS precursors (Fig. 4). We use a short time window to limit the interference between the $S_{\mathrm{LAB}}S$ wave and the main SS wave. Example amplitude measurement experiments using synthetic data show that amplitude ratios at the measurement frequency as well as their frequency-dependent variations can be well captured using a 40-second time window (Fig. 5). We will focus on measurements at a period of 25 seconds in this study. The longest half duration of the earthquakes used in this study is about 25 seconds and seismic energy often decreases rapidly at frequencies higher than

the earthquake corner frequency. In addition, SS precursors at higher frequencies can be heavily contaminated by noises (meteorological and multiple scattering). At periods much longer than 25 seconds, seismograms are not suitable for SS precursor studies as the precursors are not well separated and surface-wave overtone dispersion also becomes a problem. The frequency dependence of the measurements and their corresponding finite-frequency sensitivities will be documented in a separate paper. Amplitude ratios $S_{\rm LAB}S/S_{410}S$ and $S_{\rm LAB}S/S_{660}S$ are calculated for the observed datasets as well as synthetic seismograms in 1-D reference models (Fig. 6).

We measure the differential arrival times between the SS waves and their precursors in the dataset. The observed and synthetic seismograms are aligned using the SS traveltime measurements, and the residue arrival times of the SS precursors are then calculated in the frequency domain at a period of 25 seconds (Xue et al., 2015) (Fig. 7). The time shifts due to uncertainties in source origin times do not affect the final measurements as only $\delta t|_{S_{\rm LAB}S} - \delta t|_{SS}$ and $\delta t|_{S_{220}S} - \delta t|_{SS}$ differential traveltimes are used to determine the depths of the discontinuities. The length of the measurement windows ranges from 42 to 117 seconds for SS waves, 37 to 69 seconds for $S_{\rm LAB}S$ waves and 38 to 75 seconds for $S_{220}S$ waves. The length of a measurement window depends on the arrivals of the neighboring phases, and the measurement windows are chosen to minimize possible phase interferences. The relation between time delays and depth perturbations of the discontinuities depends on their finite-frequency sensitivity kernels. We calculate finite-frequency traveltime sensitivities to boundary depth perturbations in the framework of travelling-wave mode coupling, which fully account for source radiation patterns, phase interactions as well as time-domain windowing and tapering applied in making frequency-dependent measurements (Deng & Zhou, 2015; Zhou, 2009; Zhou et al., 2005). Example finite-frequency boundary sensitivity kernels for traveltime measurements are plotted in Fig. 4. The finite-frequency sensitivities display a typical X shape due to the minimax-time nature of the reflected waves (Dahlen, 2005). Unlike direct body waves which have minimum-time ray paths, surface-reflected phases are minimax waves in that the reflection point is a stationary maximum for perturbations in the source-receiver ray plane and a minimum for perturbations perpendicular to the plane.

Seismic waves at different frequencies are sensitive to different regions (Fresnel zones) and this introduces frequency-dependent time shifts when lateral variations exist in discon-

tinuity topography, as a result, SS precursors do not always have the same polarities as expected for 1-D earth models (Guo & Zhou, 2020). The interferences between different waves within the measurement window are accounted for in the calculation of the finite-frequency sensitivities, including the travel time curves of the interference phases as well as their amplitudes. We use traveltime sensitivity kernels to identify possible phase interferences in the measurement windows, including interferences with the main SS waves and other phases such as the precursors of depth phases (Fig. S5), precursors and/or multiples of ScS waves (Fig. S6). Sensitivity kernels with abnormal values indicate strong interferences and those measurements are excluded (Figs S5 & S6). In addition, we exclude measurements out of the two standard deviations. This leaves 1274 and 929 sets of measurements for $S_{\mathrm{LAB}}S$ and $S_{220}S$, respectively. The thicknesses of the asthenosphere at the 921 locations are calculated as the depth difference between the 220-km discontinuity and the LAB.

3 Results

We process a total number of 32,369 transverse component seismograms that have reflection points in oceanic regions and observe clear SS waves on 6,143 seismograms with simple source time functions. SS precursors are secondary reflected waves, their amplitudes are much smaller than the main SS waves and they are often heavily influenced by scattered waves and phase interactions. As expected, the majority of the seismograms with clear SS waves do not show strong SS precursors from the two discontinuities. The most striking observation from this dataset is the anomalously large amplitudes of the $S_{\mathrm{LAB}}S$ phases on 1,380 seismograms, with the majority (1,021 out of 1,380) accompanied by strong $S_{220}S$ phases. The SS precursors are well separated from the main SS waves, and their amplitudes are comparable to the amplitudes of the mantle transition zone phases, $S_{410}S$ and $S_{660}S$ (Fig. 1). The geographic distribution of the reflection points is dispersive across major oceans, including the Pacific, the Atlantic and the Indian ocean, with seafloor age spanning from 10 to 170 million years old (Fig. 1).

3.1 Large Amplitudes of the LAB *SS* precursors

To quantify the observed large amplitudes of the SS precursors associated with the LAB discontinuity, we calculate the amplitude ratios between the $S_{\mathrm{LAB}}S$ phase and two reference phases, $S_{410}S$ and $S_{660}S$. The amplitude measurements are made in the frequency

194 domain based on spectra division at a period of 25 seconds (Guo & Zhou, 2020; Xue et
195 al., 2015), In Fig. 6, we plot the histograms of the minimum amplitude ratios, defined as
196 $\gamma = \text{minimum}[\log(A_{S_{\text{LAB}}S}/A_{S_{410}S}), \log(A_{S_{\text{LAB}}S}/A_{S_{660}S})]$ (Table S1). We have used the min-
197 imum values to avoid over amplification when the amplitude of $S_{410}S$ or $S_{660}S$ is small due
198 to scattering or defocusing. The precursors $S_{\text{LAB}}S$ and $S_{410}S$ (or $S_{660}S$) have similar ray
199 paths in the bulk mantle, the use of amplitude ratios minimizes the impact of possible focus-
200 ing and defocusing effects. In addition, the main SS waves travel through the same regions
201 sampled by the SS precursors, and the distribution the SS amplitude measurements for the
202 entire dataset is very similar to that for the subset in which anomalously large $S_{\text{LAB}}S$ were
203 observed, indicating that the observed large amplitudes of the $S_{\text{LAB}}S$ waves are not a result
204 of focusing caused by mantle heterogeneities (Fig. S7). To investigate possible interference
205 from the main SS waves and other phases on the frequency-domain $S_{\text{LAB}}S$ amplitude mea-
206 surements, we make additional time-domain amplitude measurements using the maximum
207 value of the envelope function for each $S_{\text{LAB}}S$ measurement window. The measurements
208 made in the frequency domain based on spectra division and those made in the time domain
209 using envelope functions in general agree well (Fig. S8). The observed mean value of the
210 minimum amplitude ratio γ is close to zero (Fig. 6), indicating that the reflection coeffi-
211 cients at the LAB are about the same as those at the 410 and the 660. The corresponding
212 velocity contrasts across the LAB are expected to be larger than the contrasts across the 410
213 and the 660 due to their smaller incident angles at shallower depths. The geographic dis-
214 tribution of the amplitude ratios do not show dependence on the age of the sea floor (Fig. 6).
215

216 To estimate the velocity change across the LAB, we construct a 1-D reference model
217 with the depths of the LAB and the 220-km discontinuity at 130 km and 250 km, respec-
218 tively (Fig. 3). The velocity jump across the LAB is 12.5% in the reference model (Model
219 I). SS precursors from all upper mantle discontinuities can be clearly identified on the ob-
220 served seismograms when the observed and synthetic seismograms are filtered to the same
221 frequency band (Fig. 1). We make amplitude measurements and calculate the relative am-
222 plitude ratios $\gamma = \text{minimum}[\log(A_{S_{\text{LAB}}S}/A_{S_{410}S}), \log(A_{S_{\text{LAB}}S}/A_{S_{660}S})]$ using the synthetic
223 seismograms following the same process as applied on the observed seismograms. The am-
224 plitude ratios between $S_{\text{LAB}}S$ and $S_{410}S$ (or $S_{660}S$) calculated for Model I are very close
225 to the observations (Fig. 6). To better constrain the velocity drop across the LAB required
226 to produce the large amplitudes of $S_{\text{LAB}}S$, we introduce two additional models, Model II

with 6% of velocity drop and Model III with 11% of velocity drop across the LAB. Example synthetic seismograms are plotted in Fig. 3 and the amplitude measurements are plotted in Fig. 6. The mean logarithm amplitude ratio γ calculated using Model II as a reference model is -0.3, meaning that the corresponding average amplitudes of the LAB precursors are about 50% of the amplitudes of the 410 (or the 660) precursors, much smaller than the observations. The mean logarithm amplitude ratio γ calculated using Model III as a reference model is slightly smaller than the observed value. Based on the calculations, we conclude that 12.5% of velocity drop across the LAB is necessary in our model to explain the observed large amplitude of the $S_{\mathrm{LAB}}S$ waves (Fig. 6).

3.2 Depths of the LAB and the 220-km Discontinuity

To constrain the depths of the LAB and the 220-km discontinuity, we measure the differential traveltimes $\delta t|_{S_{\mathrm{LAB}}S} - \delta t|_{SS}$ and $\delta t|_{S_{220}S} - \delta t|_{SS}$ with respect to synthetic seismograms calculated in Model I (Fig. 7), similar to the studies of Guo & Zhou (2020, 2021) in which $S_{410}S$ and $S_{660}S$ traveltime measurements were used to investigate the depths of the 410-km and the 660-km discontinuities at a global scale. The time shifts due to uncertainties in source origin times do not affect the final measurements as we use differential traveltimes. We apply 3-D crust and mantle wave speed corrections using global models CRUST1.0 (Laske et al., 2013) and S40RTS (Ritsema et al., 2011). Model I is constructed as the reference model for the oceanic regions where large-amplitude SS precursors have been observed. As it is not a global reference model, there is overall about 5 seconds of traveltime shifts in $\delta t|_{S_{\mathrm{LAB}}S}$-$\delta t|_{SS}$ after 3-D wavespeed and crustal corrections (Fig. 7 & Fig. S9). The mean $\delta t|_{S_{220}S}$-$\delta t|_{SS}$ traveltime delay before and after the corrections remains approximately the same, with an average value close to zero. This indicate that the average velocity in the uppermost mantle in the reference model is close to the global average.

To obtain depth perturbations of the LAB and the 220-km discontinuity, we calculate the sensitivities of the differential traveltimes to depth perturbations of the interfaces by integrating the finite-frequency sensitivity kernels over the surface of the boundary (Fig. 4). The LAB depths obtained from this study varies between ∼70 and ∼160 km (Fig. 8) and the mean LAB depths obtained using the same data with and without the corrections are 120 km and 125 km, respectively (Figs. 8 & S10). The depth of the 220-km discontinuity

varies between 180 and 340 km with a mean value of ∼255 km, and it does not change with wavespeed and crustal corrections. We calculate the thickness of the asthenosphere in regions where both the LAB and the 220-km discontinuities are well defined by strong SS precursors from both discontinuities. The thickness of the asthenosphere ranges from 50 km to 220 km with an average of 140 km. Large depth variations of the LAB and the 220-km discontinuity are observed across the global oceanic regions and the depth can change abruptly over small geographic distances.

The depths of the LAB and the 220-km discontinuity are plotted as a function of seafloor age in Fig. 9. The depths of the two discontinuities obtained using the same dataset but without the 3-D crustal and mantle wave speed corrections are plotted in Fig. S11. The average depth of the two discontinuities are independent of seafloor age, regardless of the corrections applied. To quantify uncertainties in traveltime measurements and discontinuity depth perturbations, we calculate frequency-dependent traveltime measurements at five different periods ranging from 23 to 27 seconds. The standard deviation of those traveltime measurements are then converted to uncertainties in discontinuity depth using the corresponding finite-frequency sensitivities. The depth uncertainties are plotted as error bars in Fig. 9, they are generally small, with an average of 1.1 km for the LAB and 1.2 km for the 220-km discontinuity.

4 Discussions

4.1 Melt Spots in the Oceanic Asthenosphere

The observed large amplitudes of the SS precursors require a large velocity change across the LAB. The presence of a small amount of melt may significantly reduce seismic velocity. It has been suggested that S-wave velocity reduction is about 7.9% for every percent of melt in realistically shaped melt in the upper mantle based on finite element calculations for shear modulus reduction (produced by the presence of a connected network of realistically shaped and naturally organized melt inclusions), with the geometries of the inclusions taken directly from laboratory calculations (Hammond & Humphreys, 2000). The finite element model predictions are also in general agreement with recent experimental results (Chantel et al., 2016). The large amplitudes of the SS precursors observed in this study can be explained by 1.5%-2% of melt in the asthenosphere. This melt concentration is

comparable to observations at mid-ocean ridges, for example, the East Pacific Rise (Team, 1998). In a recent surface-wave study (Debayle et al., 2020), a large melt fraction of up to 1% beneath the entire oceanic lithosphere has been suggested, in general agreement with the overall estimation of melt (0.3-2%) from electrical conductivity study (Ni et al., 2011).

A sharp increase in the water content across the LAB has been proposed as a possible candidate for significant wave speed reduction through enhanced anelasticity (Karato, 2012; Karato & Jung, 1998). To explore the effect of anelasticity (seismic quality factor Q) on the amplitudes of SS precursors, we calculate synthetic seismograms in models with and without strong anelasticity in the asthenosphere and compare the amplitudes of the SS precursors. In Fig. 10, the velocity and density structures in Model I and Model IV are identical but their Q values in the asthenosphere are different, Q=80 in Model I and Q=20 in Model IV. The low Q value in the asthenosphere in Model IV results in a much smaller SS amplitude but the amplitude reduction on the $S_{\rm LAB}S$ wave is very limited. This is because while both the SS wave and the $S_{\rm LAB}S$ wave experience more attenuation due to enhanced anelasticity, anelasticity also reduces the effective wave speed in the low Q region. Therefore, the effective velocity contrast across the LAB increases, resulting a larger reflection coefficient and increased amplitude of the $S_{\rm LAB}S$ wave. The amplitude ratios calculated in Model I (Fig. 6) and Model IV (Fig. 10) do not show significant differences in their histograms. We conclude that the large amplitudes of $S_{\rm LAB}S$ waves therefore can not be explained by a change in anelasticity.

The observed large amplitudes of the SS precursors can not be explained by seismic anisotropy. Strong radial anisotropy (up to 10%) has been observed in the oceanic asthenosphere with SH waves travelling faster than SV waves (Dziewonski & Anderson, 1981; Zhou et al., 2006; Nettles & Dziewoński, 2008; Burgos et al., 2014; Beghein et al., 2014). This radial anisotropy would lead to larger SH wave velocity beneath the LAB, and therefore reduced velocity contrast across the LAB and smaller precursor amplitudes, while the observed large amplitudes of the SS precursors require anomalously large velocity drop (12.5%) across the boundary. Frozen-in radial anisotropy in the oceanic lithosphere from petrological fabrics or melt ponding has been suggested (Auer et al., 2015). In this case, the SH wave speed would become faster in the oceanic lithosphere, which may cause a larger SH velocity contrast across the LAB but a reduced velocity contrast in SV velocity. In this study, strong

$S_{\mathrm{LAB}}S$ phases are also observed on the radial component seismograms (Fig. S12). The observed SS precursors with large amplitudes also display a good azimuth coverage (Fig. 1), indicating that the observed large amplitudes of the $S_{\mathrm{LAB}}S$ waves are unlikely a result of azimuth anisotropy in the lithosphere (Beghein et al., 2014).

It is important to emphasize that we have interpreted the low velocity zone (LVZ) between the two discontinuities observed in oceanic regions as the asthenosphere, and we have modeled the wavespeed structure associated with reflected waves as first-order discontinuities. In 1-D earth models (e.g., PREM), a first-order discontinuity is an equivalent mathematical representation of the earth structure. The same applies to other discontinuities in the Earth including the Moho, the 410 and the 660. Synthetic seismograms calculated based on the equivalent first-order discontinuities can explain the observed seismograms. The large amplitude of the LAB phase observed in this study requires about 12.5% of velocity jump across a first-order discontinuity. The same velocity change over a gradient zone of 5 km or less may also explain the observed $S_{\mathrm{LAB}}S$ amplitudes, with less than 2% of difference in their average amplitudes (Fig. S13). If the velocity change occurs over a much larger gradient zone of 20 km, the average $S_{\mathrm{LAB}}S$ amplitude will decrease by $\sim$17%, and the required velocity increase would be larger in order to produce the same peak amplitude (Deng & Zhou, 2015).

4.2 Age-Independent Thickness of the Oceanic Plate

The observed LAB SS precursors characterized by large amplitudes can be modeled as waves reflected off a first-order discontinuity with a large velocity contrast. The strong SS precursors from the LAB are observed across the global oceanic regions, with an average depth of 120 km that is independent of seafloor age (Fig. 9). This observation supports the plate model for the oceanic bathymetry and heat flow measurements, in which a reheating process is required at the base of the oceanic plate with a constant thickness of about 100-125 km. The reheating process is probably caused by small-scale mantle convection beneath the large oceanic plate (Richards et al., 2020).

The observed depths of the LAB in this study are characterized by substantial local variations. The standard deviation of the LAB depths calculated for the entire dataset is

at ∼15 km. We calculate the standard deviation of the LAB depths at different length scales (Fig. S14). The standard deviation can be up to ∼17 km at small length scales and it becomes consistent with the standard deviation of the entire dataset when the length scale exceeds ∼1000 km. Reflectors at depths between 120 and 180 km have been detected across the Pacific ocean in a *SS* precursor stacking study, though they were found in only 16% of the stacks (Schmerr, 2012). LAB reflectors at depths of about 100-140 km have been reported in Hawaii where high-resolution receiver function studies are available with the deployment of local stations (Li et al., 2000, 2004). The large variation of the LAB depths is also consistent with surface waves studies in which individual transects often display considerable depth variability in age-averaged profiles (Rychert et al., 2020; French et al., 2013).

In seismic studies, age-dependent reflectors have been reported in several oceanic regions, especially under the young seafloors (Rychert et al., 2021; Rychert & Shearer, 2011; Tharimena et al., 2017; Wang et al., 2020). For example, a recent receiver function study from ocean bottom seismometers in the equatorial Mid Atlantic Ocean discovered that the LAB depth increases from about 30 km at the mid-ocean ridge to about 80 km beneath 30 million years old seafloors in some locations (Rychert et al., 2021). The relation between the crust age and the LAB depth is much less clear across the Pacific Ocean and it has been suggested that regional dynamical processes may play an important role in asthenospheric melt production (Schmerr, 2012). In this study, we use long period SS waves, as a result, signals from a very shallow reflector (<40 km) will interfere with the main SS waves and will not be picked up. It is also possible that there may be multiple reflectors in the lithosphere in some regions and what we observe in this study represents a strong deep reflector associated with melting not secular cooling. In general, velocity change associated with a thermal lithosphere is expected to be smaller and much more gradual than the reflectors associated with the chemical differentiation (melting) process.

Similar to the LAB, the depths of the 220-km discontinuity also do not depend on the age of the seafloor and are characterized with large local variations. It is understood that the smoothness (roughness) of a same discontinuity in different studies often depends on the regions of study as well as smoothing applied in some of the inversions. Reflectors at depths of 250-300 km (the X discontinuity) have been observed in many oceanic regions, including the South Pacific and the Indian Ocean (Deuss & Woodhouse, 2002, 2004). Large depth

variations up to ∼100 kilometers on the 220-km discontinuity have been report over length scales of several hundred kilometers beneath the northwestern Pacific in a short-period array study (Rost & Weber, 2001). The large local variations in the depths of the discontinuities are expected to generate significant variability in both the waveforms and travel times of the SS precursors. When stacking is applied to SS precursors with reflection points in regions where large depth variations occur over very short distances, it may be possible that the large amplitudes of SS precursors could be effectively averaged out in stacking results due to phase equalization (Gu et al., 2001). In Fig. S14, we show a simple example to illustrate the concept that, in some cases, the large amplitudes of SS precursors may not be picked up in stacking results when large variations in SS precursor amplitudes and arrival times are present.

5 Conclusions

The thermal boundary as predicted by the half space cooling model is not observed in SS precursors in this study. Instead, we observe anomalously large amplitudes of SS precursors reflected off the lithosphere-asthenosphere boundary (LAB), which can be explained by ∼12.5% of velocity drop across the boundary. This indicates 1.5%-2% of localized melt across the global oceanic regions. The large variability in the depths and amplitudes of the SS precursors observed across the global oceanic region suggests a heterogeneous melting process in the oceanic asthenosphere. The majority of the LAB SS precursors are accompanied by strong reflections from the 220-km discontinuity. This indicates that the 220-km discontinuity may define the lower boundary of the local asthenosphere where melting occurs.

The plate model, which requires additional heat at the base of a constant-thickness oceanic plate, explains the bathymetry and heat flow observations that do not follow half space cooling predictions. While such a constant-thickness plate has not been reported in seismic studies, the oceanic plate as defined by the strong LAB reflector in this study does not thicken with age but show an average depth of 120 km across different age bands. This observation supports the existence of a constant-thickness plate in oceanic regions. The localized melt spots distributed over the global oceanic regions may be essential to decouple the oceanic plates from the underlying mantle by dramatically reducing the mantle viscosity

418 (Debayle et al., 2020; Holtzman, 2016).

419

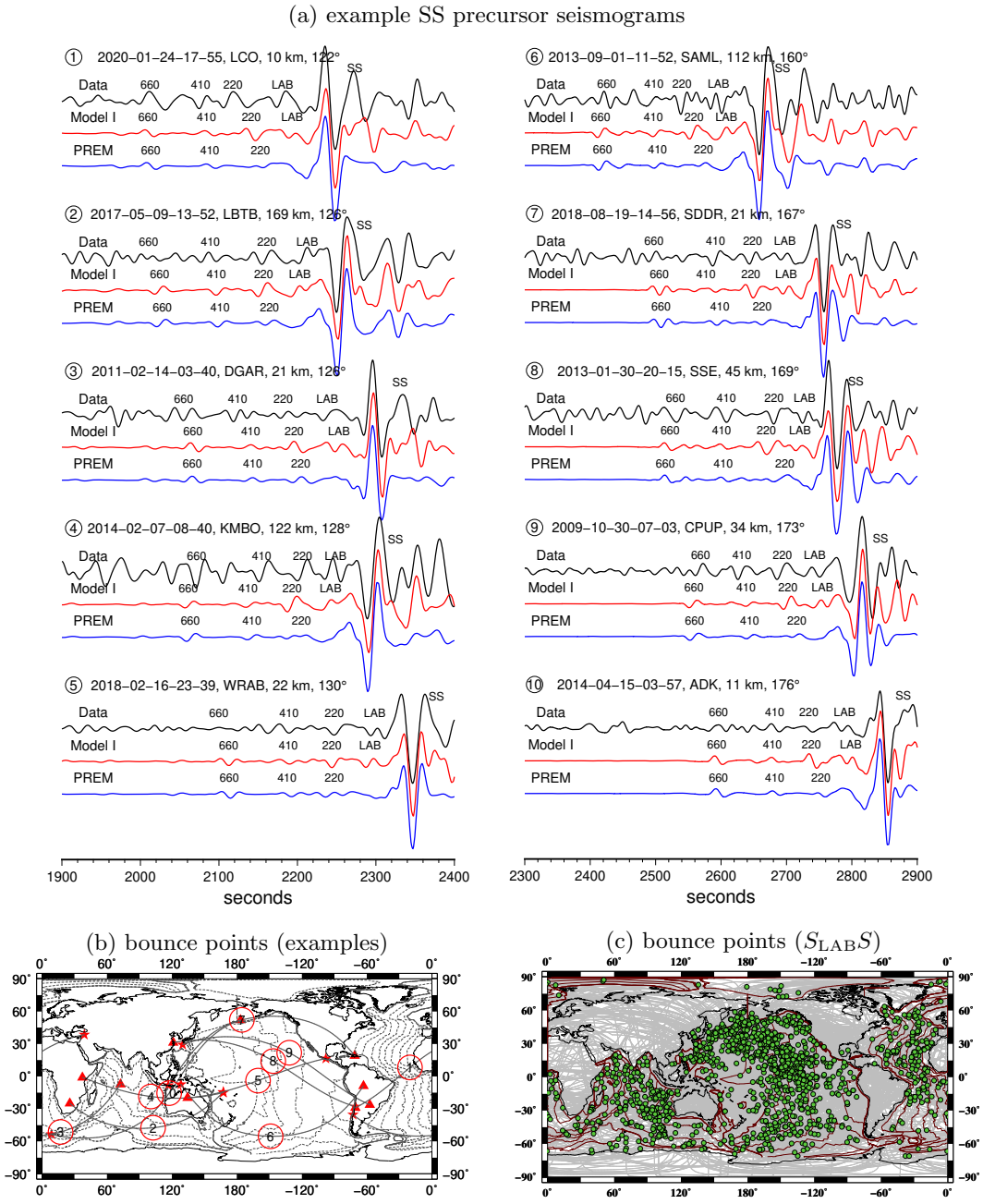

Figure 1: (a) example transverse-component seismograms with large-amplitude $S_{\mathrm{LAB}}S$ and $S_{220}S$ phases. The black seismograms are data, the red seismograms are synthetics calculated in a reference 1-D model (Model I) with 12.5% of the velocity jump across the LAB, and the blue synthetics are calculated in PREM in which there is no discontinuity at the LAB depth. The reference models are plotted in Fig. 3. The seismograms have been band-pass filtered between 10 and 80 mHz and aligned using their SS arrivals for better illustration. The precursor closest to the main SS wave is labeled as $S_{\mathrm{LAB}}S$ as we investigate possible reflections from the top of the asthenosphere. The arrivals of the $S_{220}S$, $S_{410}S$ and $S_{660}S$ waves are also labeled. The earthquake event date/time and station name as well as depth and epicentral distance are denoted on each seismogram. The corresponding geographic ray paths (black lines) and bounce points (red circles) of the $S_{\mathrm{LAB}}S$ waves are plotted in (b). Ray paths and bounce points of the 1,380 $S_{\mathrm{LAB}}S$ waves with anomalously large amplitudes are plotted in (c). Seafloor age contours are plotted at 20, 60, 100 and 140 Ma.

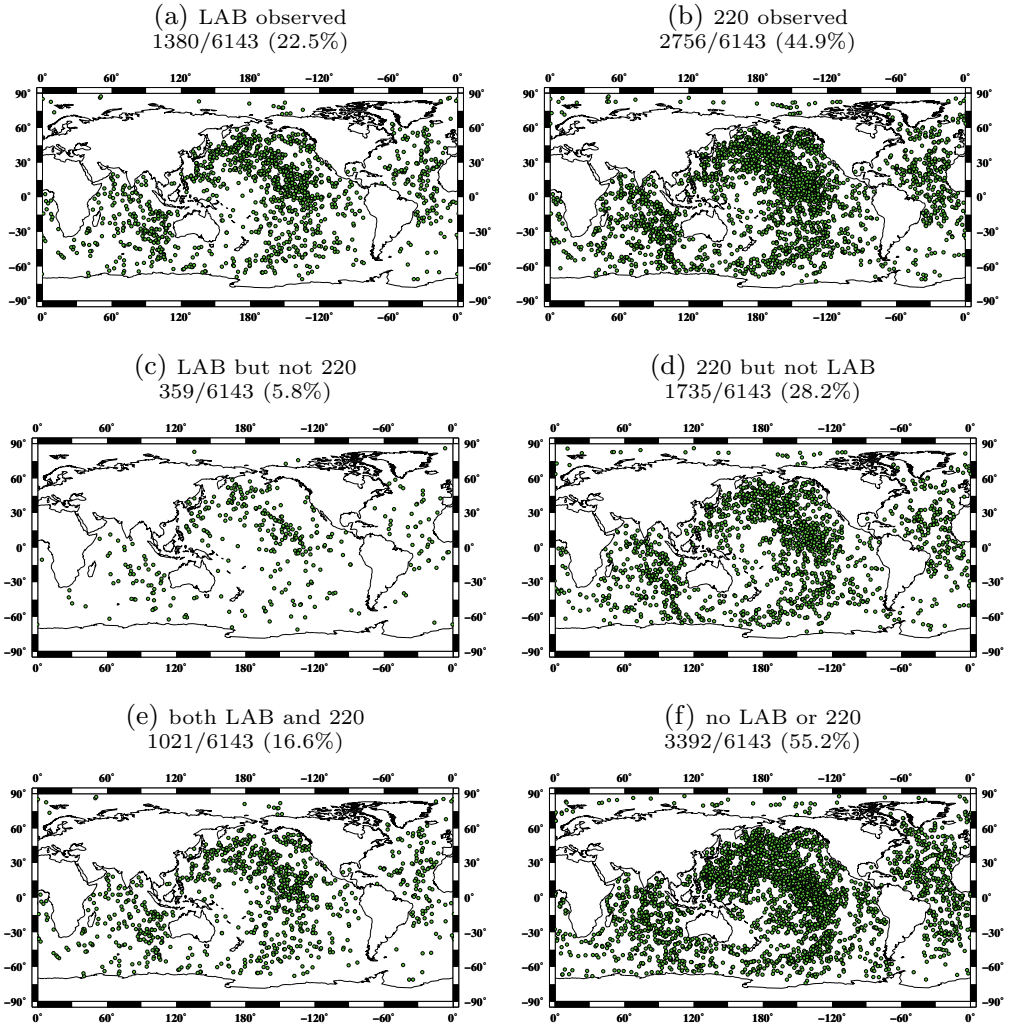

Figure 2: Geographic distribution of subsets of the data plotted at SS bounce points. (a) clear $S_{\mathrm{LAB}}S$ observed, (b) clear $S_{220}S$ observed, (c) $S_{\mathrm{LAB}}S$ observed but not $S_{220}S$, (d) $S_{220}S$ observed but not $S_{\mathrm{LAB}}S$, (e) both $S_{\mathrm{LAB}}S$ and $S_{220}S$ observed, (f) no $S_{\mathrm{LAB}}S$ or $S_{220}S$ observed. There is no apparent geographic pattern associated with either the presence or absence of the $S_{\mathrm{LAB}}S$ and $S_{220}S$.

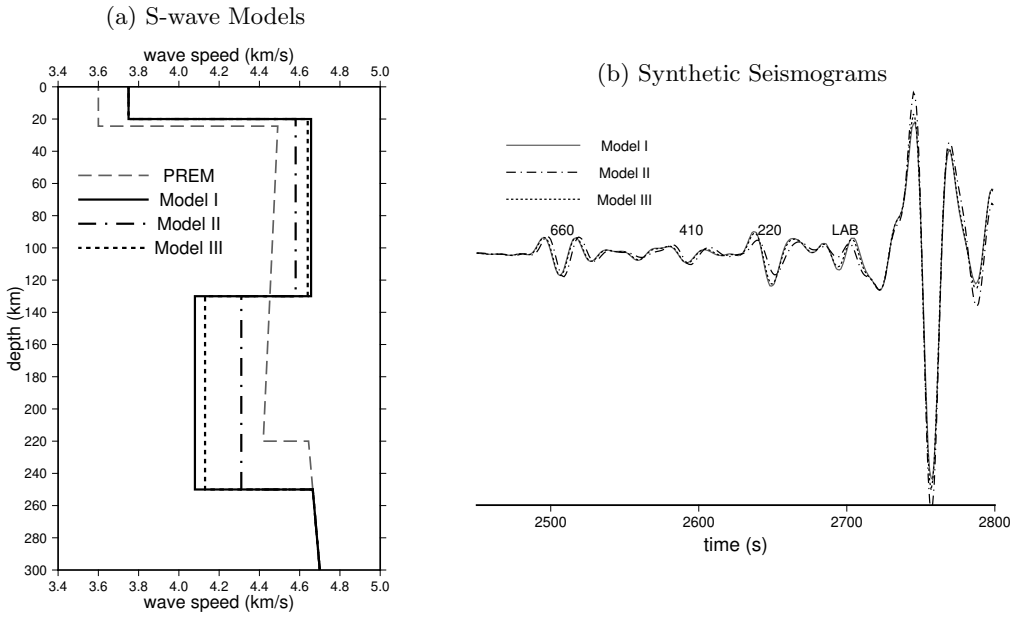

Figure 3: (a) Three 1-D reference earth models Model I, Model II and Model III used in this study and their corresponding example synthetic seismograms are plotted in (b). Model PREM is also plotted in (a) for reference. The synthetic seismograms are calculated using the three reference models for a magnitude 6.9 Indonesia earthquake occurred in August 2018 recorded at a GSN station SDDR (https://doi.org/10.7914/SN/CU). The observed seismogram is plotted in Fig. 1. The seismograms have been band-pass filtered between 10 and 80 mHz and have been aligned using the main SS wave arrivals for better illustration. The velocity contrast across the LAB at a depth of 130 km is 12.5% in Model I, 6% in Model II and 11% in Model III. The corresponding $S_{\mathrm{LAB}}S$ wave amplitude in Model I is much larger than that in Model II and slightly larger than that in Model III, as expected.

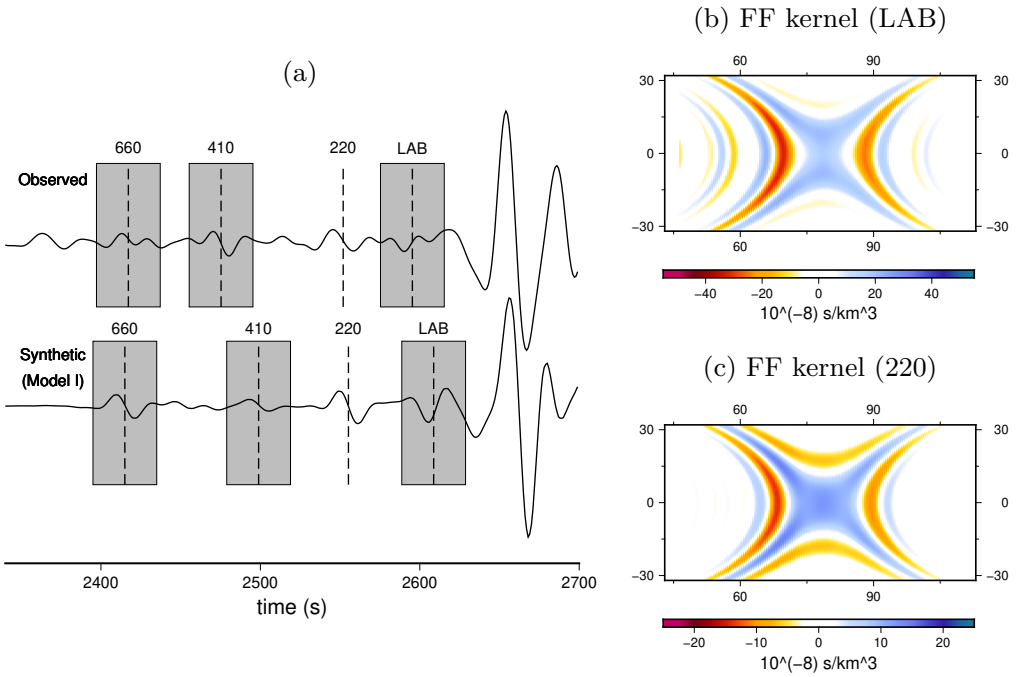

Figure 4: (a) shows example measurement windows used for LAB amplitude ratio measurements $A_{S_{\mathrm{LAB}}S}/A_{S_{410}S}$ and $A_{S_{\mathrm{LAB}}S}/A_{S_{660}S}$. The seismograms are for a magnitude 6.6 Mexico earthquake occurred in January 2016 recorded at a GSN station MSEY (https://doi.org/10.7914/SN/II), and the epicentral distance is 158°. The synthetic seismogram is calculated for Model I as in Fig. 3 and both seismograms have been band-pass filtered between 10 and 80 mHz. (b) and (c) are finite-frequency traveltime boundary sensitivity kernels for the $S_{\mathrm{LAB}}S$ and $S_{220}S$ waves, respectively. The sensitivity kernels are plotted in map view in the ray coordinates, centered at the bounce point which is about 79° away from the source and the receiver.

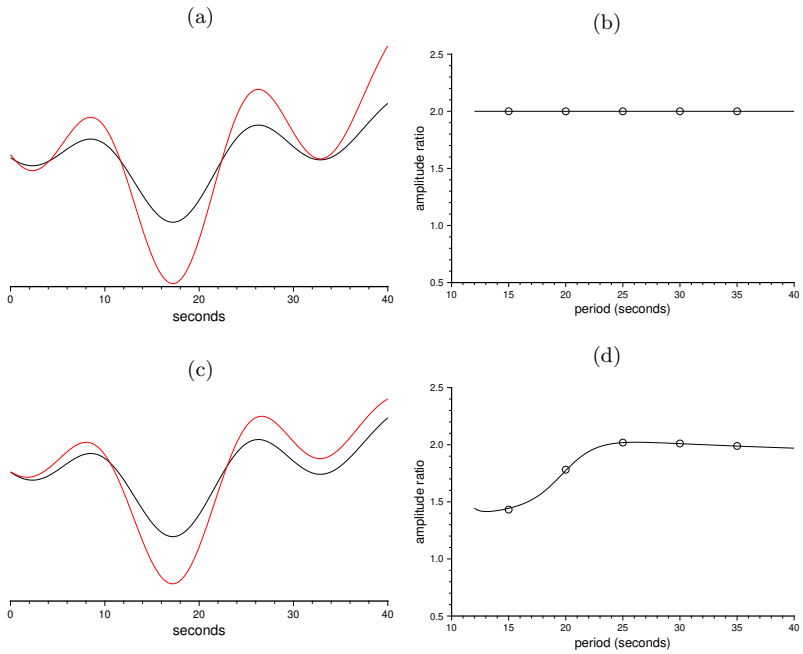

Figure 5: Synthetic amplitude measurement experiment using the same 40-second time window as applied in data. (a) The black seismogram is the LAB phase from the observed seismogram in Fig. 4, and we multiply the seismogram by a constant factor of two (frequency-independent) to obtain the red seismogram. (b) Theoretical amplitude spectral ratio (black line) and measurements made at periods of 15, 20, 25, 30 and 35 seconds (circles). (c) The black seismogram is the same as in (a) and the red seismogram is obtained by multiplying the amplitude spectrum of the black seismogram with a frequency-dependent function. The corresponding theoretical amplitude ratios and measurements made at 15, 20, 25, 30 and 35 seconds period are plotted in (d). The experiment confirms that amplitude ratios at the measurement frequency (25 seconds) can be determined using a 40-second time window.

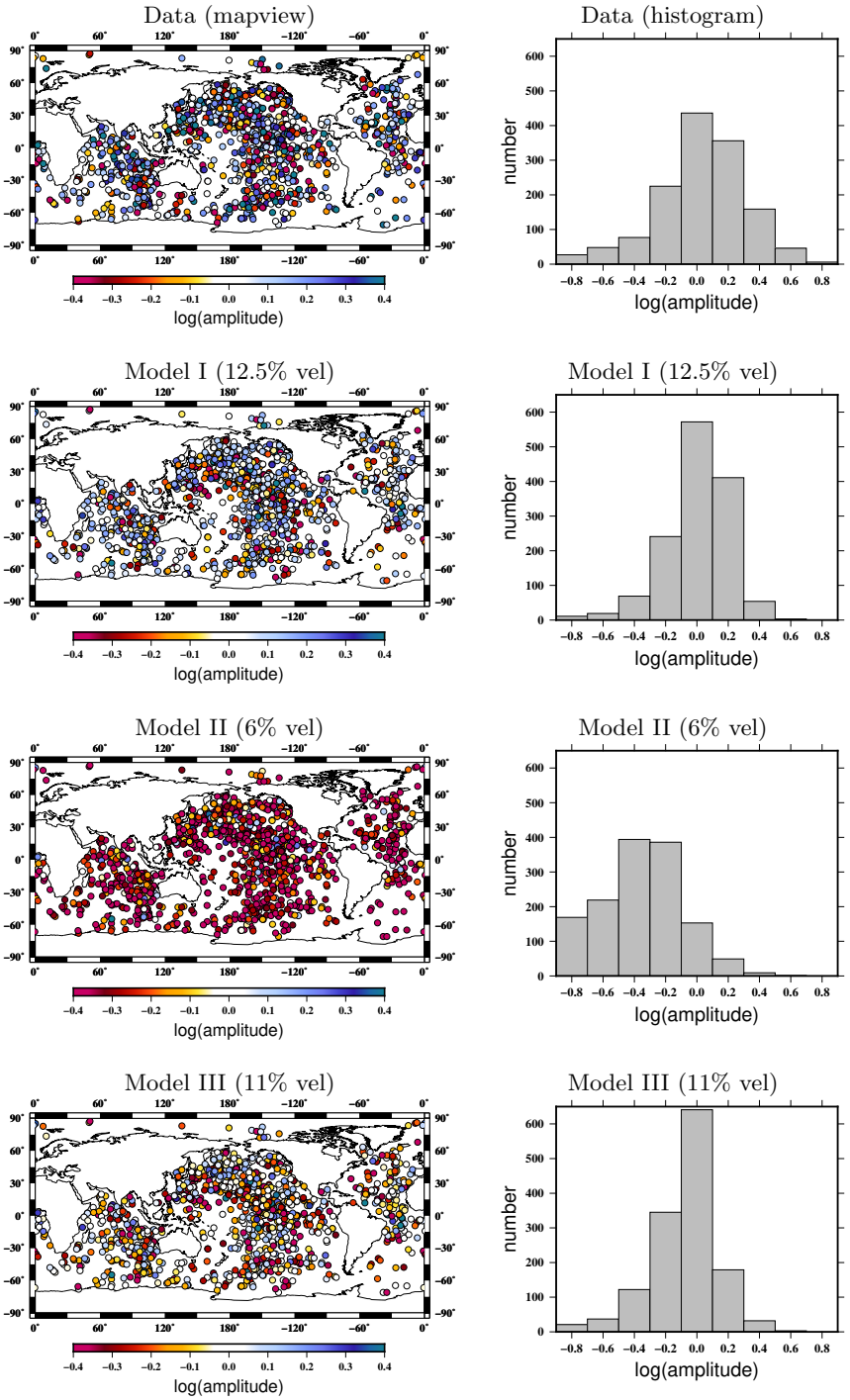

Figure 6: $S_{\rm LAB}S$ amplitude measurements γ = minimum $[\log(A_{S_{\rm LAB}S}/A_{S_{410}S}), \log(A_{S_{\rm LAB}S}/A_{S_{660}S})]$ obtained using observed seismograms (top) as well as synthetic seismograms calculated for three reference models (Model I, II and III) plotted at the bounce points in mapviews and histograms. The observed $S_{\rm LAB}S$ amplitudes show a similar distribution (histogram) to the amplitude ratios calculated for Model I (12.5% velocity drop across the LAB). The amplitude ratios calculated in Model II (6% velocity drop across the LAB) are overall much smaller than the observations, and the amplitude ratios calculated in Model III (11% velocity drop across the LAB) are slightly smaller than the observed amplitude ratios. We conclude that the observed large amplitude of the $S_{\rm LAB}S$ waves can be explained by 12.5% of velocity drop across the LAB.

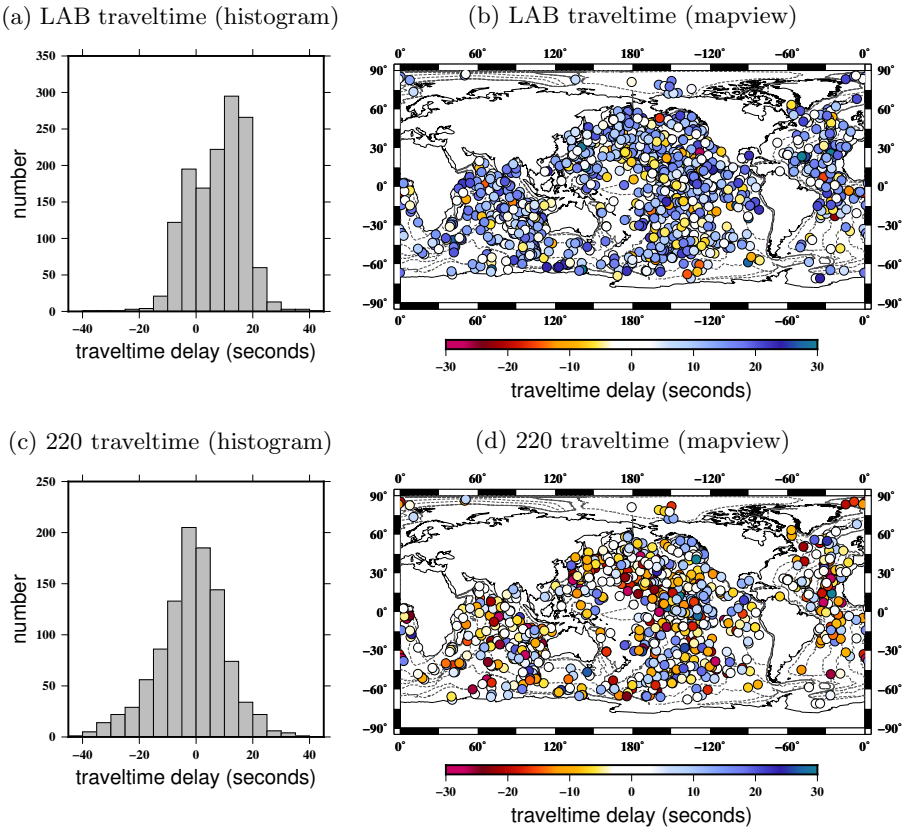

Figure 7: (a) and (b) are $S_{\mathrm{LAB}}S$ traveltime measurements plotted in histograms and mapviews at their bounce points. The measurements are made with respect to Model I synthetic seismograms. 3-D mantle wavespeed and crustal corrections have been applied. (c) and (d) are the same as (a) and (b) but for $S_{220}S$.

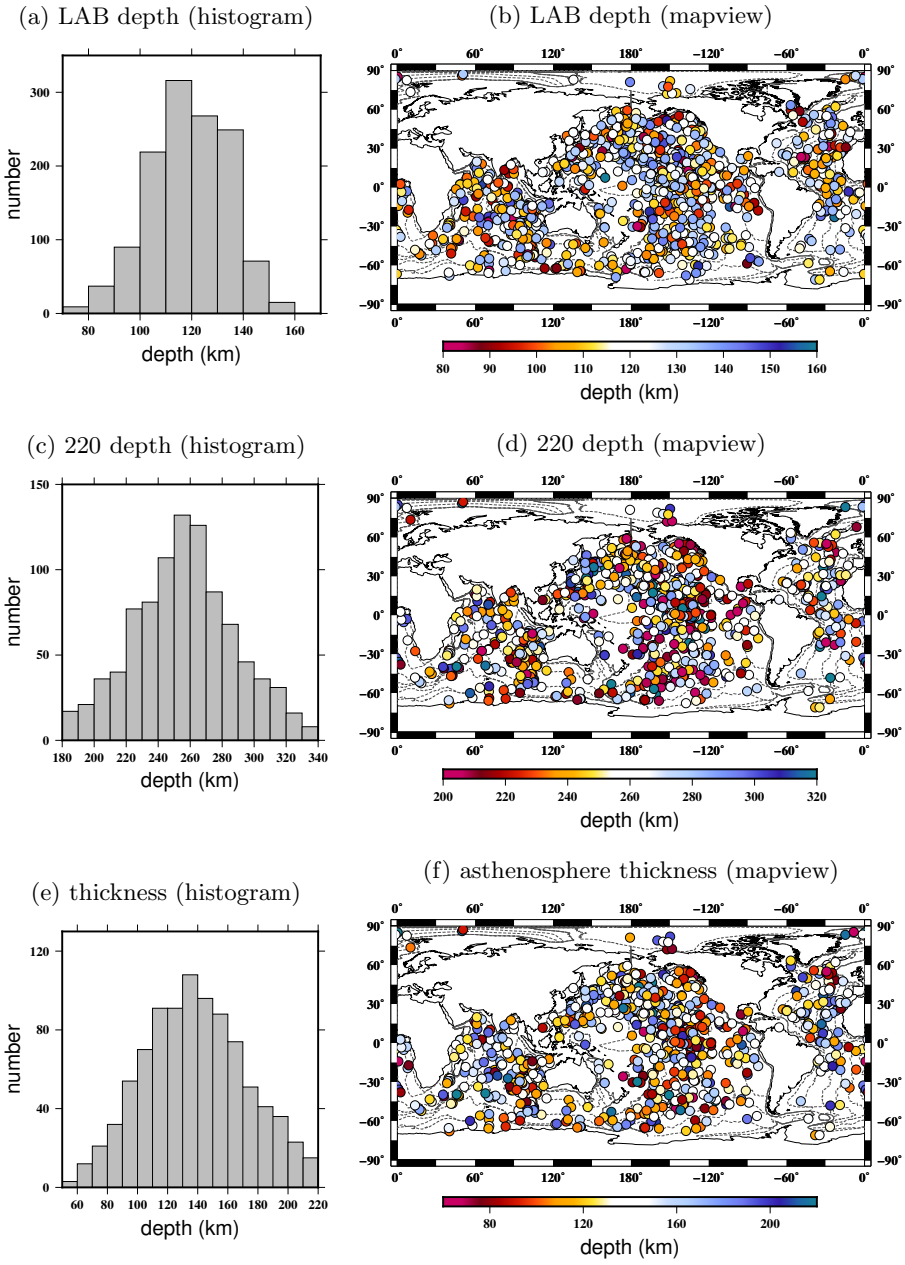

Figure 8: (a) and (b) are the depths of the LAB calculated from traveltime measurements, plotted in histogram and mapview at $S_{\mathrm{LAB}}S$ bounce points. (c) and (d) are the depths of the 220-km discontinuity. (e) and (f) are the asthenosphere thicknesses calculated from the depths of the LAB and the 220.

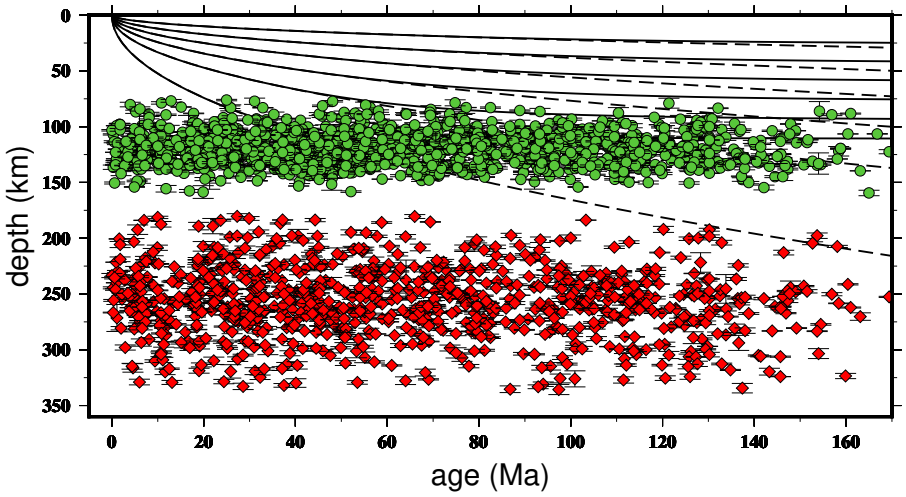

Figure 9: **Age-independent thickness of the oceanic plate.** Green circles and red diamonds are depths of the LAB and the 220-km discontinuity obtained from this study, plotted as a function of the seafloor age. Isotherms at an interval of 200°C (starting at 300°C) from the half space cooling model (dashed line) and the plate model (solid line) are plotted for reference. The observed depths of the two discontinuities show significant local variations. The average depths of the LAB and the 220-km discontinuity are at 120 km and 255 km, independent of seafloor age. The depth uncertainties estimated from frequency-dependent measurements are plotted as error bars.

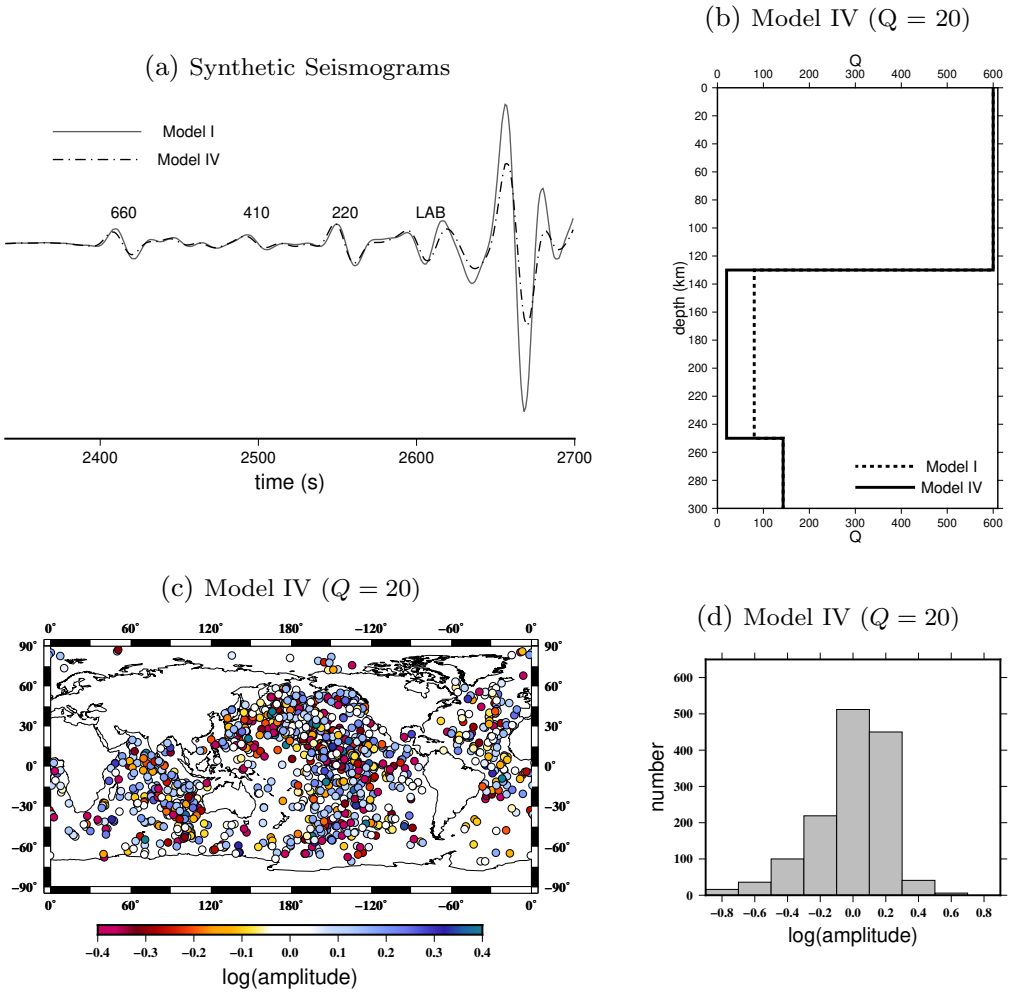

Figure 10: (a) Synthetic seismograms calculate for Model I and Model IV as in Fig. 3. (b) Q structure in the 1-D reference models Model I and Model IV. Model IV is identical to Model I in velocity and density but has a much smaller Q value (Q=20) in the asthenosphere than in Model I (Q=80). The amplitude of the main SS wave becomes smaller in Model IV synthetics due to the overall stronger attenuation associated with the lower Q value in the asthenosphere but its impact on the amplitude of the SS precursor $S_{\rm LAB}S$ is very limited. This is because anelasticity also reduces the effective wave speed in the low Q region. Therefore, velocity contrast across the LAB increases, resulting a larger reflection coefficient which increases the amplitude of the $S_{\rm LAB}S$ wave. The observed large amplitudes of the $S_{\rm LAB}S$ waves therefore can not be fully explained by a reduction of Q values in the asthenosphere.

Acknowledgments

We thank the Editor Dr. Douglas Schmitt, the Associate Editor and an anonymous reviewer for their constructive comments, which helped improve the manuscript. The facilities of the IRIS Data Management System, and specifically the IRIS Data Management Center, were used for access to waveform and metadata required in this study. The authors acknowledge Advanced Research Computing at Virginia Tech for providing computational resources and technical support. This research was supported by the US National Science Foundation under Grant EAR-2017218.

Data Availability Statement

Raw seismic waveforms used in this study are available from the IRIS platform (https://ds.iris.edu/ds/nodes/dmc/). All GSN stations were used (Network codes are CU, GT, IC, II, IU). Data preparation and preprocessing were performed using the Seismic Analysis Code (https://ds.iris.edu/ds/nodes/dmc/software/downloads/sac/). Figures were made with the Generic Mapping Tools (GMT) package (Wessel & Smith, 1995).

References

Auer, L., Becker, T. W., Boschi, L., & Schmerr, N. (2015). Thermal structure, radial anisotropy, and dynamics of oceanic boundary layers. *Geophysical Research Letters*, *42*(22), 9740–9749.

Beghein, C., Yuan, K., Schmerr, N., & Xing, Z. (2014). Changes in seismic anisotropy shed light on the nature of the gutenberg discontinuity. *Science*, *343*(6176), 1237–1240.

Burgos, G., Montagner, J.-P., Beucler, E., Capdeville, Y., Mocquet, A., & Drilleau, M. (2014). Oceanic lithosphere-asthenosphere boundary from surface wave dispersion data. *Journal of Geophysical Research: Solid Earth*, *119*(2), 1079–1093.

Chantel, J., Manthilake, G., Andrault, D., Novella, D., Yu, T., & Wang, Y. (2016). Experimental evidence supports mantle partial melting in the asthenosphere. *Science Advances*, *2*(5), e1600246. doi: 10.1126/sciadv.1600246

Dahlen, F. (2005). Finite-frequency sensitivity kernels for boundary topography perturbations. *Geophysical Journal International*, *162*(2), 525–540.

Debayle, E., Bodin, T., Durand, S., & Ricard, Y. (2020). Seismic evidence for partial melt below tectonic plates. *Nature*, *586*(7830), 555–559.

Deng, K., & Zhou, Y. (2015). Wave diffraction and resolution of mantle transition zone discontinuities in receiver function imaging. *Geophysical Journal International*, *201*(3), 2008–2025.

Deuss, A., & Woodhouse, J. H. (2002). A systematic search for mantle discontinuities using ss-precursors. *Geophysical Research Letters*, *29*(8), 90–1.

Deuss, A., & Woodhouse, J. H. (2004). The nature of the lehmann discontinuity from its seismological clapeyron slopes. *Earth and Planetary Science Letters*, *225*(3-4), 295–304.

Dziewonski, A. M., & Anderson, D. L. (1981). Preliminary reference earth model. *Physics of the earth and planetary interiors*, *25*(4), 297–356.

Faul, U. H., & Jackson, I. (2005). The seismological signature of temperature and grain size variations in the upper mantle. *Earth and Planetary Science Letters*, *234*(1-2), 119–134.

Fischer, K. M., Ford, H. A., Abt, D. L., & Rychert, C. A. (2010). The lithosphere-asthenosphere boundary. *Annual Review of Earth and Planetary Sciences*, *38*, 551–575.

Fischer, K. M., Rychert, C. A., Dalton, C. A., Miller, M. S., Beghein, C., & Schutt, D. L. (2020). A comparison of oceanic and continental mantle lithosphere. *Physics of the Earth and Planetary Interiors*, 106600.

French, S., Lekic, V., & Romanowicz, B. (2013). Waveform tomography reveals channeled flow at the base of the oceanic asthenosphere. *Science*, *342*(6155), 227–230.

Gaherty, J. B., & Jordan, T. H. (1995). Lehmann discontinuity as the base of an anisotropic layer beneath continents. *Science*, *268*(5216), 1468–1471.

Godfrey, K. E., Dalton, C. A., & Ritsema, J. (2017). Seafloor age dependence of rayleigh wave phase velocities in the indian ocean. *Geochemistry, Geophysics, Geosystems*, *18*(5), 1926–1942.

Goncz, J. H., & Cleary, J. R. (1976). Variations in the structure of the upper mantle beneath australia, from rayleigh wave observations. *Geophysical Journal International*, *44*(2), 507–516.

Gu, Y. J., Dziewonski, A. M., & Ekström, G. (2001). Preferential detection of the lehmann discontinuity beneath continents. *Geophysical Research Letters*, *28*(24), 4655–4658.

Guo, Z., & Zhou, Y. (2020). Finite-frequency imaging of the global 410-and 660-km discontinuities using ss precursors. *Geophysical Journal International*, *220*(3), 1978–1994.

Guo, Z., & Zhou, Y. (2021). Stagnant slabs and their return flows from finite-frequency tomography of the 410-km and 660-km discontinuities. *Journal of Geophysical Research: Solid Earth*, *126*(5), e2020JB021099.

Hales, A., Muirhead, K., & Rynn, J. (1980). A compressional velocity distribution for the upper mantle. *Tectonophysics*, *63*(1-4), 309–348.

Hammond, W. C., & Humphreys, E. D. (2000). Upper mantle seismic wave velocity: Effects of realistic partial melt geometries. *Journal of Geophysical Research: Solid Earth*, *105*(B5), 10975–10986.

Holtzman, B. K. (2016). Questions on the existence, persistence, and mechanical effects of a very small melt fraction in the asthenosphere. *Geochemistry, Geophysics, Geosystems*, *17*(2), 470–484.

James, E. K., Dalton, C. A., & Gaherty, J. B. (2014). Rayleigh wave phase velocities in the a tlantic upper mantle. *Geochemistry, Geophysics, Geosystems*, *15*(11), 4305–4324.

Karato, S.-i. (1992). On the lehmann discontinuity. *Geophysical Research Letters*, *19*(22), 2255–2258.

Karato, S.-i. (2012). On the origin of the asthenosphere. *Earth and Planetary Science Letters*, *321*, 95–103.

Karato, S.-i., & Jung, H. (1998). Water, partial melting and the origin of the seismic low velocity and high attenuation zone in the upper mantle. *Earth and Planetary Science*

Letters, *157*(3-4), 193–207.

Karato, S.-i., & Wu, P. (1993). Rheology of the upper mantle: A synthesis. *Science*, *260*(5109), 771–778.

Kawakatsu, H., Kumar, P., Takei, Y., Shinohara, M., Kanazawa, T., Araki, E., & Suyehiro, K. (2009). Seismic evidence for sharp lithosphere-asthenosphere boundaries of oceanic plates. *Science*, *324*(5926), 499–502.

Kawakatsu, H., & Utada, H. (2017). Seismic and electrical signatures of the lithosphere–asthenosphere system of the normal oceanic mantle. *Annual Review of Earth and Planetary Sciences*, *45*.

Korenaga, T., & Korenaga, J. (2008). Subsidence of normal oceanic lithosphere, apparent thermal expansivity, and seafloor flattening. *Earth and Planetary Science Letters*, *268*(1-2), 41–51.

Laske, G., Masters, G., Ma, Z., & Pasyanos, M. (2013). Update on crust1. 0—a 1-degree global model of earth's crust. In *Geophys. res. abstr* (Vol. 15, p. 2658).

Lehmann, I. (1959). Velocities of longitudinal waves in the upper part of the earth's mantle. In *Annales de géophysique* (Vol. 15, p. 93).

Lehmann, I. (1961). S and the structure of the upper mantle. *Geophysical Journal International*, *4*(Supplement_1), 124–138.

Li, X., Kind, R., Priestley, K., Sobolev, S. V., Tilmann, F., Yuan, X., & Weber, M. (2000). Mapping the hawaiian plume conduit with converted seismic waves. *Nature*, *405*(6789), 938–941.

Li, X., Kind, R., Yuan, X., Wölbern, I., & Hanka, W. (2004). Rejuvenation of the lithosphere by the hawaiian plume. *Nature*, *427*(6977), 827–829.

Liu, K., & Zhou, Y. (2016). Travelling-wave green tensor and near-field rayleigh-wave sensitivity. *Geophysical Supplements to the Monthly Notices of the Royal Astronomical Society*, *205*(1), 134–145.

Ma, Z., & Dalton, C. A. (2019). Evidence for dehydration-modulated small-scale convection in the oceanic upper mantle from seafloor bathymetry and rayleigh wave phase velocity. *Earth and Planetary Science Letters*, *510*, 12–25.

Maggi, A., Debayle, E., Priestley, K., & Barruol, G. (2006). Multimode surface waveform tomography of the pacific ocean: a closer look at the lithospheric cooling signature. *Geophysical Journal International*, *166*(3), 1384–1397.

Mehouachi, F., & Singh, S. C. (2018). Water-rich sublithospheric melt channel in the

equatorial atlantic ocean. *Nature Geoscience*, *11*(1), 65–69.

Nettles, M., & Dziewoński, A. M. (2008). Radially anisotropic shear velocity structure of the upper mantle globally and beneath north america. *Journal of Geophysical Research: Solid Earth*, *113*(B2).

Ni, H., Keppler, H., & Behrens, H. (2011). Electrical conductivity of hydrous basaltic melts: implications for partial melting in the upper mantle. *Contributions to Mineralogy and Petrology*, *162*(3), 637–650.

Parsons, B., & Sclater, J. G. (1977). An analysis of the variation of ocean floor bathymetry and heat flow with age. *Journal of geophysical research*, *82*(5), 803–827.

Revenaugh, J., & Jordan, T. H. (1991). Mantle layering from scs reverberations: 3. the upper mantle. *Journal of Geophysical Research: Solid Earth*, *96*(B12), 19781–19810.

Richards, F., Hoggard, M., Crosby, A., Ghelichkhan, S., & White, N. (2020). Structure and dynamics of the oceanic lithosphere-asthenosphere system. *Physics of the Earth and Planetary Interiors*, 106559.

Richter, F. M. (1973). Convection and the large-scale circulation of the mantle. *Journal of Geophysical Research*, *78*(35), 8735–8745.

Richter, F. M., & Parsons, B. (1975). On the interaction of two scales of convection in the mantle. *Journal of Geophysical Research*, *80*(17), 2529–2541.

Ritsema, J., Deuss, a. A., Van Heijst, H., & Woodhouse, J. (2011). S40rts: a degree-40 shear-velocity model for the mantle from new rayleigh wave dispersion, teleseismic traveltime and normal-mode splitting function measurements. *Geophysical Journal International*, *184*(3), 1223–1236.

Rost, S., & Weber, M. (2001). A reflector at 200 km depth beneath the northwest pacific. *Geophysical Journal International*, *147*(1), 12–28.

Rychert, C. A., Harmon, N., Constable, S., & Wang, S. (2020). The nature of the lithosphere-asthenosphere boundary. *Journal of Geophysical Research: Solid Earth*, *125*(10), e2018JB016463.

Rychert, C. A., Schmerr, N., & Harmon, N. (2012). The pacific lithosphere-asthenosphere boundary: Seismic imaging and anisotropic constraints from ss waveforms. *Geochemistry, Geophysics, Geosystems*, *13*(9).

Rychert, C. A., & Shearer, P. M. (2009). A global view of the lithosphere-asthenosphere boundary. *Science*, *324*(5926), 495–498.

Rychert, C. A., & Shearer, P. M. (2011). Imaging the lithosphere-asthenosphere boundary

beneath the pacific using ss waveform modeling. *Journal of Geophysical Research: Solid Earth*, *116*(B7).

Rychert, C. A., Tharimena, S., Harmon, N., Wang, S., Constable, S., Kendall, J. M., ... Schlaphorst, D. (2021). A dynamic lithosphere–asthenosphere boundary near the equatorial mid-atlantic ridge. *Earth and Planetary Science Letters*, *566*, 116949.

Sacks, I., Snoke, J., & Husebye, E. (1979). Lithosphere thickness beneath the baltic shield. *Tectonophysics*, *56*(1-2), 101–110.

Schmerr, N. (2012). The gutenberg discontinuity: Melt at the lithosphere-asthenosphere boundary. *Science*, *335*(6075), 1480–1483.

Schmerr, N., & Garnero, E. (2006). Investigation of upper mantle discontinuity structure beneath the central pacific using ss precursors. *Journal of Geophysical Research: Solid Earth*, *111*(B8).

Shearer, P. M. (1991). Constraints on upper mantle discontinuities from observations of long-period reflected and converted phases. *Journal of Geophysical Research: Solid Earth*, *96*(B11), 18147–18182.

Stern, T., Henrys, S. A., Okaya, D., Louie, J. N., Savage, M. K., Lamb, S., ... Iwasaki, T. (2015). A seismic reflection image for the base of a tectonic plate. *Nature*, *518*(7537), 85–88.

Team, T. M. S. (1998). Imaging the deep seismic structure beneath a mid-ocean ridge: The melt experiment. *Science*, *280*(5367), 1215–1218.

Tharimena, S., Rychert, C., Harmon, N., & White, P. (2017). Imaging pacific lithosphere seismic discontinuities—insights from ss precursor modeling. *Journal of Geophysical Research: Solid Earth*, *122*(3), 2131–2152.

Turcotte, D., & Oxburgh, E. (1967). Finite amplitude convective cells and continental drift. *Journal of Fluid Mechanics*, *28*(1), 29–42.

Turcotte, D. L., & Schubert, G. (2002). *Geodynamics*. Cambridge university press.

Vidale, J. E., & Benz, H. M. (1992). Upper-mantle seismic discontinuities and the thermal structure of subduction zones. *Nature*, *356*(6371), 678–683.

Wang, S., Constable, S., Rychert, C. A., & Harmon, N. (2020). A lithosphere-asthenosphere boundary and partial melt estimated using marine magnetotelluric data at the central middle atlantic ridge. *Geochemistry, Geophysics, Geosystems*, *21*(9), e2020GC009177.

Wessel, P., & Smith, W. H. F. (1995). New version of the generic mapping tools released. *Eos Trans. AGU*, *76*, 329.

Xue, J., Zhou, Y., & Chen, Y. J. (2015). Tomographic resolution of plume anomalies in the lowermost mantle. *Geophysical Journal International*, *201*(2), 979–995.

Yamauchi, H., & Takei, Y. (2016). Polycrystal anelasticity at near-solidus temperatures. *Journal of Geophysical Research: Solid Earth*, *121*(11), 7790–7820.

Zhou, Y. (2009). Multimode surface wave sensitivity kernels in radially anisotropic earth media. *Geophysical Journal International*, *176*(3), 865–888.

Zhou, Y., Dahlen, F., Nolet, G., & Laske, G. (2005). Finite-frequency effects in global surface-wave tomography. *Geophysical Journal International*, *163*(3), 1087–1111.

Zhou, Y., Nolet, G., Dahlen, F. A., & Laske, G. (2006). Global upper-mantle structure from finite-frequency surface-wave tomography. *Journal of Geophys. Res.*, *111*, doi:10.1029/2005JB003677.